

# High-Resolution NMR Spectroscopy at Large Fields with Nitrogen Vacancy Centers

C. Munuera-Javaloy,<sup>1,2</sup> A. Tosalina,<sup>1,2</sup> and J. Casanova<sup>1,2,3</sup>

<sup>1</sup>Department of Physical Chemistry, University of the Basque Country UPV/EHU, Apartado 644, 48080 Bilbao, Spain

<sup>2</sup>EHU Quantum Center, University of the Basque Country UPV/EHU, Leioa, Spain

<sup>3</sup>IKERBASQUE, Basque Foundation for Science, Plaza Euskadi 5, 48009 Bilbao, Spain

Ensembles of nitrogen-vacancy (NV) centers are used as sensors to detect NMR signals from micron-sized samples at room temperature. In this scenario, the regime of large magnetic fields is especially interesting as it leads to a large nuclear thermal polarisation –thus, to a strong sensor response even in low concentration samples– while chemical shifts and J-couplings become more accessible. Nevertheless, this regime remains largely unexplored owing to the difficulties to couple NV-based sensors with high-frequency nuclear signals. In this work, we circumvent this problem with a method that maps the relevant energy shifts in the amplitude of an induced nuclear spin signal that is subsequently transferred to the sensor. This stage is interspersed with free-precession periods of the sample nuclear spins where the sensor does not participate. Thus, our method leads to high spectral resolutions ultimately limited by the coherence of the nuclear spin signal.

**Introduction.**– Nuclear magnetic resonance (NMR) is a fundamental technique for a variety of areas such as diagnosis medicine, biochemistry, and analytical chemistry [1, 2]. From its inception in 1946 [3–5] NMR has grown to constitute, nowadays, its own research area [9]. The discussion over the optimal field strength has been present in the field for several decades [6], and the profits provided by elevated magnetic fields of the order of several Teslas—namely, increased spatial and spectral resolutions—have long been known [7, 8]. As other disciplines, NMR has experienced, in recent years, a profitable symbiosis with the rapidly growing field of quantum technologies [10]. In particular, the use of newly-developed solid-state quantum sensors [11], such as NV centers in diamond [12], has enabled to interrogate ever smaller samples [13–15]. This has led to NMR experiments that provide unprecedented spatial resolutions, even to the limit of single molecule addressing [16–18]. In this regard, the benefits of operating at large magnetic fields are expected to carry on for NMR analysis of micro and nanoscale sized samples with quantum sensors.

Nuclear spins are main actors in NMR as they are the source of the target magnetic signal. The evolution of a nucleus in an external magnetic field is also affected by the distribution of nearby magnetic sources such as electrons in chemical bounds. Consequently, detecting the resulting variations in the Larmor precession frequency through NMR procedures –thus, leading to precise information about J-couplings and chemical shifts– serves as an accurate diagnosis of the molecular structure around target nuclei. Identifying these changes, even at considerably large magnetic fields, requires measurement protocols that achieve frequency resolutions of the order of Hz. However, the spectral resolution of standard quantum sensing techniques is severely limited by the coherence time of the sensor. In the case of NV centers, this restriction leads to kHz resolutions even when the sensor is stabilised with dynamical decoupling techniques [19], leading to an insufficient record for useful chemical analysis.

Recently, protocols capable of overcoming these limitations have been devised. With techniques that resemble classical heterodyne detection, measurements of artificial signals us-

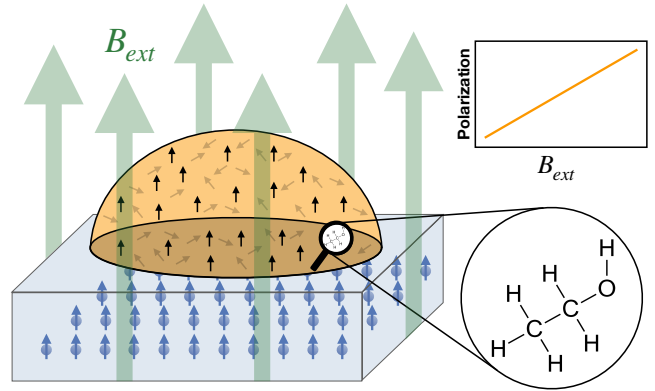


FIG. 1. The setup consists on a picoliter sized sample placed on top of a diamond substrate. The diamond contains an NV ensemble as the sensor of the magnetic signal generated by the analyte. The protons of the studied molecule emit a signal with a frequency that depends on their local electronic/dipolar environment, thus carrying structural information.

ing NV probes [20, 21] reached  $\mu$ Hz resolution. In addition, when applied to micron sized samples these techniques have led to detection of J-couplings and chemical shifts at low magnetic fields [22]. These applications, however, suffer from low sensitivity caused by the weakness of the nuclear signals, imposing the need for large amount of repetitions headed to an averaged final result. Besides, these protocols can be deployed only in samples with a large hydrogen concentration such that they provide sufficiently intense signals, thus limiting their utility for competitive chemical analysis.

A possible workaround to this limitation proposes to increment the polarization of the sample previous to the detection protocol using dynamical nuclear polarization techniques, hence achieving stronger signals and improved contrasts [23, 24]. Alternatively, operating at large static magnetic fields would enhance the thermal polarisation, increasing the NMR signal intensity without adding new compounds to the sample, hence enabling to interrogate samples in a wide range of concentrations (not only with highly concentrated ones).

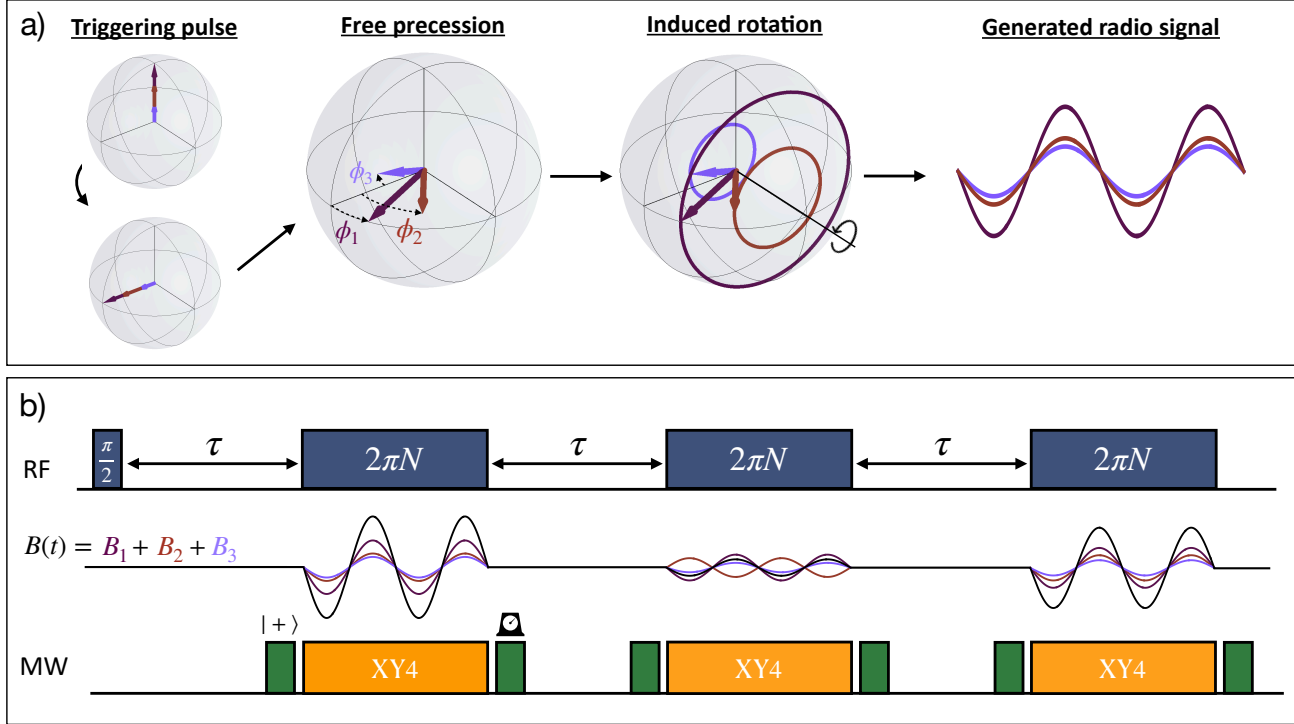


FIG. 2. Portrait of the custom signal production and measurement. a) An initial RF  $\pi/2$  pulse brings the sample thermal polarization to the orthogonal plane and triggers the AERIS protocol consisting on free precessions and induced rotations stages. For a time  $\tau$  each magnetization vector  $\mathbf{M}_k(t)$  precess according to the local field at the position of the nuclear spin. The phase covered by each  $\mathbf{M}_k(t)$  –this is  $\phi_k = \delta_k\tau$ – is encoded in the amplitude of the oscillating field generated via controlled rotations of these vectors. b) (First panel) RF control sequence with interleaved free precessions. (Second panel) Sample emitted fields. These have different amplitudes due to the distinct projections of each rotating  $\mathbf{M}_k(t)$  on the  $Z$  axis. The depicted case shows three  $B_i$  fields as a consequence of the splitting among three magnetization vectors that spin at rates  $\delta_1$ ,  $\delta_2$ , and  $\delta_3$ . (Third panel) MW pattern –in our case an XY4 dynamical decoupling sequence– on each NV devised to capture the induced signal. Note that the NVs remain inactive during the long free precession stages of the sample, providing our protocol with increased spectral resolution regardless of the sensor coherence time. Prior to the dynamical decoupling operation, the NV ensemble is initialized in  $|+\rangle$  while once its state encodes the desired information it is optically readout in the  $|\sigma_y\rangle$  basis.

Besides, the presence of large magnetic fields would facilitate the identification of frequency changes caused by the local environment of nuclei, as J-couplings become clearer and chemical shifts increase.

In this Letter we present the AERIS (Amplitude-Encoded Radio Induced Signal) method. This is a detection protocol for solid-state quantum sensors able to handle large magnetic field scenarios and that achieves a spectral resolution which is only limited by the coherence time of the nuclear spin signal, thus leading to a spectral resolution compatible with chemical shifts and J-couplings. We exemplify the AERIS method with NV centers, however this is equally applicable to other types of solid-state-based sensors such as those appearing in silicon carbide substrates [25, 26]. Moreover, the method might be combined with recently used dynamical nuclear polarization techniques [23, 24, 27, 28] leading to stronger target signals, thus further reducing the need to average over the outcomes of various realizations.

*The protocol.*– State of the art NV-based AC field magnetometry typically target the oscillating signal produced by pre-

cessing nuclear spins, whose frequency is proportional to the local field felt by the nuclei. On the one hand, this relation allows to acquire information on the molecular environment of the nuclei by unraveling the spectral composition of the signal. On the other hand, when the sample is exposed to a large magnetic field, it leads to signals that oscillate too fast to be traced by the NV. Note that approaches based on the delivery of appropriately shaped pulses have been proposed for dealing with moderate field scenarios, or in situations where only reduced MW power is available [29, 30]. Here we take an alternative approach and target a deliberately manufactured signal that carries the spectroscopic information of the studied sample encoded in its amplitude rather than in its frequency.

We consider a thermally polarized sample placed on top of an NV-ensemble-based-sensor and in the presence of a large external magnetic field  $B_{ext}$ , see Fig (1). The depth of the considered NV defects permits to neglect statistical fluctuations of the polarization [22]. The sample would contain a certain type of molecule with nuclear spins in different locations of its structure. Hereafter we use subindex  $k$  (or superindex when

required by the notation) to indicate the different precession frequencies produced by distinct local magnetic fields. This scenario is similar to those reported in [22–24] with the critical difference of the magnitude of  $B_{ext}$ .

Following [2] we describe the spins of our sample through the nuclear magnetization  $\mathbf{M} = (M_x, M_y, M_z)$ . This is a dimensionless, time-dependent vector proportional to the average nuclear magnetic moment of the sample. Its behavior during a RF pulse of intensity  $\Omega$  in a frame that rotates with the frequency of the RF driving ( $\omega$ ) is described by the Bloch equations

$$\frac{d}{dt} \begin{pmatrix} M_x \\ M_y \\ M_z \end{pmatrix} = \begin{pmatrix} -1/T_2 & -\delta & \Omega \sin \phi \\ \delta & -1/T_2 & -\Omega \cos \phi \\ -\Omega \sin \phi & \Omega \cos \phi & -1/T_1 \end{pmatrix} \begin{pmatrix} M_x \\ M_y \\ M_z \end{pmatrix} + \begin{pmatrix} 0 \\ 0 \\ 1/T_1 \end{pmatrix}, \quad (1)$$

where  $\phi$  is the phase of the RF field and  $T_1$  ( $T_2$ ) is the relaxation (dephasing) rate of the nuclear sample. The detuning  $\delta = \omega_L - \omega$  between the RF pulse frequency and the Larmor precession rate  $\omega_L$  depends on the local magnetic field at the nuclear spin site, which differs from  $B_{ext}$  depending on the magnetic environment around the nucleus. Hence, the sample comprises  $k$  different precession frequencies  $\omega_L^k$  leading to  $k$  different detunings  $\delta_k$ .

Our AERIS protocol comprises two parts. The first one creates a detectable signal by exploiting the dynamics described in Eq. (1). This is achieved with an RF triggering pulse on the sample followed by a subsequent alternation between free precession periods and induced rotations as shown in Fig. (2). The second part consists on probing the produced signal with NV sensors that acquire a phase determined by its amplitude, gathering in their spin state information about the spectral composition of the signal and allowing to determine the local magnetic environment around nuclear spins.

More in detail: An RF pulse along the X axis (i.e.  $\phi = 0$ ) of duration  $\pi/(2\Omega)$ , see Eq. (1), tilts the initial thermal polarization of the sample,  $\mathbf{M} = (0, 0, 1)$  (note that  $\mathbf{M}$  provides the direction of the thermal polarization when it is a unit vector, and it attenuates the polarization amount as  $T_1$  and  $T_2$  diminish its modulus) to the plane perpendicular to the external field and triggers off the protocol. Once the pulse is turned off, i.e.  $\Omega = 0$  in Eq. (1), the nuclear spins coherently precess around the external field at a rate determined by the local magnetic field at their respective locations. Similar to a clock mechanism that rotates the needles representing hours, minutes and seconds at different speeds, the free precession stage of fixed duration  $\tau$  splits the magnetization vector  $\mathbf{M}(t)$  in components  $\mathbf{M}_k(t) = (\sin(\delta_k t), -\cos(\delta_k t), 0)$ . Recall,  $\delta_k$  is the detuning between the driving frequency and the  $k$ th precession frequency in the sample. Crucially, the NV sensor remains inactive at this stage, thus  $\tau$  could be significantly larger than NV coherence times leading to high spectral resolution ultimately limited by the coherence of the nuclear sample.

A longer RF pulse then continuously rotates the magnetization components at a speed  $\propto \Omega$  around an axis on the xy-plane determined by  $\phi$ , as described by Eq. (1). The pro-

jection of the resulting field in the NV axis sets a target field  $B(t)$  with two key features. Firstly, it oscillates with frequency  $\Omega \ll \omega_L$ . This is a parameter that can be tuned such that  $B(t)$  oscillations can be tracked by the NV ensemble (if this is appropriately driven with MW radiation, see later) regardless of magnetic field value acting on the sample. Secondly,  $B(t)$  comprises the radio signals produced by each rotating  $\mathbf{M}_k(t) = (\sin(\delta_k t), -\cos(\delta_k t) \cos(\Omega t), -\cos(\delta_k t) \sin(\Omega t))$ , thus it contains the footprint of each nuclear environment (encoded in the distinct  $\delta_k$  shifts). For more details see appendix (A). After  $N$  complete rotations of the magnetization vectors, thus of  $B(t)$ , the RF rotation pulse is switched off and the sample advances to the next free precession stage, in which each  $\mathbf{M}_k(t)$  continue to dephase. This sequence is iterated leading to an oscillation in the amplitudes of the signals emitted during the successive induced rotation stages, and whose spectrum relates directly to the various  $\omega_L^k$  in the sample.

The radio signal  $B_n(t)$  produced during the  $n^{th}$  induced rotation stage is captured by the NV in the ensemble such that, in a rotating frame w.r.t. the NV electronic-spin ground-state triplet, each NV evolves according to

$$H/\hbar = -\gamma_e B_n(t) \frac{\sigma_z}{2} + \Omega_{MW}(t) \frac{\sigma_\phi}{2}. \quad (2)$$

Here  $\gamma_e$  is the electronic gyromagnetic factor,  $\sigma$  are the Pauli operators of the NV two-level system, and the target signal  $B_n(t)$  is expressed in appendix (A). The control field  $\Omega_{MW}(t)$  is synchronized with the rotation pulse over nuclear spins, see Fig. (2), leading to an XY4 control sequence that allows the sensor to capture a phase determined by (i) The amplitude of the radio signal stemming from the sample, and (ii) The length of the RF pulse. This information is gathered by optically reading out the state of the sensor, with an expected result for the  $n^{th}$  phase acquisition stage of

$$\langle \sigma_y \rangle_n = \frac{2\gamma_e t_m}{\pi} \sum_k b_k \cos(\delta_k n\tau), \quad (3)$$

where  $b_k$  is the initial magnetic field amplitude on the NV site produced by the  $k^{th}$  spectral component, see appendix (A). Thus, subsequent detections provide a stroboscopic record of the oscillating amplitudes, see Fig. (3) (a), whose Fourier spectrum relates to the frequency shifts of nuclei at different sites of the sample molecule.

Let us recall that the NV ensemble sensor is only active during phase acquisition (i.e. while the dynamical decoupling sequence is active) and after that is optically readout and reinitialized. Therefore, the duration of our measuring protocol, thus its spectral resolution, gets over the cap imposed by the coherence of the sensor being only limited by the coherence of the nuclear fields. In what follows we consider a thermally polarized sample, however hyperpolarized samples [23, 24] would generate equally coherent fields and thus constitute a natural route to extend the viability of our protocol to nanoscale samples.

*Numerical Results.*— We illustrate the AERIS protocol by numerically simulating the evolution of 8 magnetization vec-

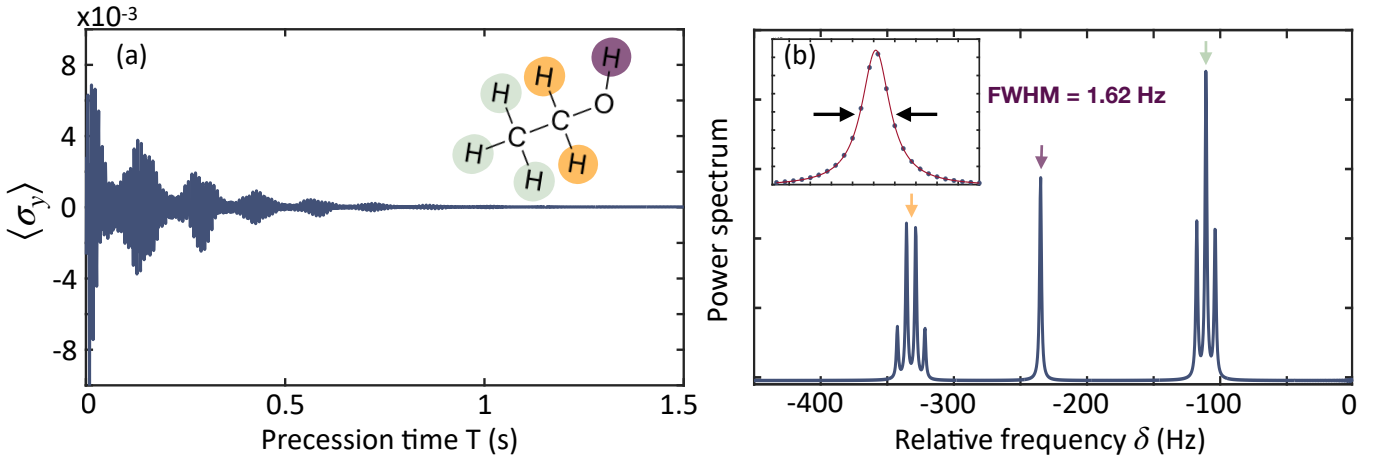


FIG. 3. Measurements and spectrum obtained by considering  $\delta_k = \{-342.45, 335.55, 328.65, 321.75, 234.9, 117.6, 110.7, 103.8\}$  Hz, and magnetic field amplitudes  $b_k = \{106, 320, 320, 106, 426, 320, 640, 320\}$  pT along the Z axis of a generic NV in the ensemble. (a) Simulated stroboscopic record collected by measuring  $\langle \sigma_y \rangle$  on the NV as a function of the cumulated precession time, after interacting with the ethanol sample (inset). The three sites of the ethanol molecule with different chemical shifts are indicated with distinct colors. (b) Fourier transform of the measurement record (blue solid line) showing peaks in the expected values. Each peak group has its origin site/chemical shift indicated with an arrow of the corresponding color. Inset, the central peak was fitted to a Lorentzian function that exhibits a full width at half maximum (FWHM) of 1.62 Hz.

tors taken from the ethanol [ $\text{C}_2\text{H}_5\text{OH}$ ] spectrum [2] in a scenario that comprises a magnetic field of 2.1 T, while the RF driving frequency  $\omega$  is set to  $(2\pi) \times 90$  MHz, which is assumed to be the origin of the chemical shift scale (this is the resonance frequency of TMS [2]). Each  $\delta_k$  detuning is obtained by considering the three chemical shifts of 3.66, 2.6, and 1.19 ppm, as well as a J-coupling of 6.9 Hz between the  $\text{CH}_3$  and the  $\text{CH}_2$  groups of ethanol [2], see caption in Fig. (3). The average field amplitude over each NV in the ensemble is estimated to  $\approx 2.56$  nT, by taking into account the proton concentration of ethanol as well as the external magnetic field of 2.1 T, see Appendix B. This field amplitude is distributed in different  $b_k$  according to the ethanol spectral structure, see caption in Fig. (3) and Appendix B. We find the radio signal emitted by the sample by numerically solving the Bloch equations during RF irradiation (i.e. at the induced rotation stages). The free precession time is  $\tau = 1$  ms, and the induced rotation stage has a duration of 40  $\mu$ s (corresponding approximately to 2 full rotations of the magnetization vectors) while the NV ensemble is controlled with an XY4 sequence. Furthermore, we use  $\Omega_{\text{MW}} = (2\pi) \times 20$  MHz,  $\Omega_{\text{RF}} = (2\pi) \times 50$  KHz, and sample coherence times  $T_1 = 2$  s and  $T_2 = 0.2$  s. This process is repeated 1500 times, leading to the stroboscopic record of Fig. (3) (a), which follows Eq. (3).

We run again the protocol by employing an initial  $\pi/2$  pulse over the Y axis leading to the sinusoidal version of Eq. (3). This is:

$$\langle \sigma_y \rangle_n = \frac{2\gamma_e t_m}{\pi} \sum_k b_k \sin(\delta_k n \tau). \quad (4)$$

Finally, both measurement records in Eqs. (3, 4) are combined and converted, via discrete Fourier transform, into the spectrum in Fig. (3) (b). There we demonstrate that the AERIS

method leads in the studied case to Lorentzian peaks with a  $\text{FWHM} \approx 1.62$  Hz (mainly limited by the sample  $T_2$ ) thus sufficient to detect the posed chemical shifts and J couplings.

*Conclusions.*— We have devised a NMR signal detection protocol that attains chemical shift level resolution from micron-sized samples, while being suitable for large magnetic fields. Our approach relies on the production of a custom field that resonates with dynamically decoupled NV sensors used to extract spectral information of the sample. Actual experiments may require several repetitions to average out the impact of shot noise or inaccurate control sequences. Nevertheless, the demand for higher spectral resolution is less stringent at large fields, as chemical shifts increase and J-couplings become clearer. Besides, polarization rates increase, leading to stronger signals that provide measurements with higher contrast. Both effects contribute to decrease the required amount of repetitions, or, conversely, to make small concentration samples amenable to our protocol, which sets the utility of NV sensors for realistic chemical analysis. Finally, our protocol could accommodate distinct upgrades, such as (i) Pre-polarization techniques that provide stronger and coherent nuclear signals even from nanoscale samples, (ii) More sophisticated dynamical decoupling techniques that augment the resilience of the operation to noise sources, and (iii) Additional RF drivings over the sample (such as Lee Goldburg [31] or WAHUHA schemes [32]) that would further contribute to remove dipolar interactions leading to cleaner spectra.

*Acknowledgements.*— We thank fruitful discussions with A. Martín. Authors acknowledge financial support from Spanish Government via EUR2020-112117, from Basque Government via the EU FET Open Grant Quromorphic (828826). C.M.-J. acknowledges the predoctoral MICINN grant PRE2019-088519. J.C. acknowledges the Ramón y

Cajal program (RYC2018-025197-I) and support from the UPV/EHU through the grant EHUrOPE.

*Note added.*- During the NanoMRI 7 conference in Barcelona, Spain, we became aware of independent work carried out in Professor Wrachtrup's group in Stuttgart that shares some characteristics with the protocol in this paper.

---

[1] A. Abragam, *The Principles of Nuclear Magnetism* (Oxford University Press, London, 1961).

[2] M. H. Levitt, *Spin Dynamics: Basics of Nuclear Magnetic Resonance*, 2nd ed. (Wiley, West Sussex, 2008).

[3] E. M. Purcell, H. C. Torrey, and R. V. Pound, *Phys. Rev.* **69**, 37 (1946).

[4] F. Bloch, W. W. Hansen, and M. Packard, *Phys. Rev.* **69**, 127 (1946).

[5] The Nobel Prize in Physics 1952.

[6] D. I. Hoult, C. N. Chen, and V. J. Sank, *Magn. Reson. Med.* **3**, 730 (1986).

[7] K. Uğurbil, G. Adriany, P. Andersen, W. Chen, M. Garwood, R. Gruetter, P. G. Henry, S. G. Kim, H. Lieu, I. Tkac, T. Vaughan, P. F. Van De Moortele, E. Yacoub, and X. H. Zhu, *Magn. Reson. Imaging* **21**, 1263 (2003).

[8] E. Moser, E. Laistler, F. Schmitt, and G. Kontaxis, *Front. Phys.* **5**, 33 (2017).

[9] E. D. Becker, *Anal. Chem.* **65**, 6, 295 (1993).

[10] J. P. Dowling, and G. J. Milburn, *Phil. Trans. R. Soc. A.* **361**, 1655 (2003).

[11] C. L. Degen, F. Reinhard, and P. Cappellaro, *Rev. Mod. Phys.* **89**, 035002 (2017).

[12] M. W. Doherty, N. B. Manson, P. Delaney, F. Jelezko, J. Wrachtrup, and L. C. L. Hollenberg, *Phys. Rep.* **528**, 1 (2013).

[13] G. Balasubramanian, I. Chan, R. Kolesov, m. Al-Hmoud, J. Tisler, C. Shin, C. Kim, A. Wojcik, P. R. Hemmer, A. Krueger, T. Hanke, A. Leitenstorfer, R. Bratschitsch, F. Jelezko, and J. Wrachtrup, *Nature* **455**, 648 (2008).

[14] P. Maletinsky, S. Hong, M. S. Grinolds B. Hausmann ,M. D. Lukin, R. L. Walsworth, M. Loncar, and A. Yacoby, *Nature Nanotech* **7**, 320 (2012).

[15] T. Staudacher, F. Shi, S. Pezzagna, J. Meijer, J. Du, C. A. Meriles, F. Reinhard, and J. Wrachtrup, *Science* **339**, 561 (2013).

[16] F. Shi, Q. Zhang, P. Wang, H. Sun, J. Wang, X. Rong, M. Chen, C. Ju, F. Reinhard, H. Chen, J. Wrachtrup, J. Wang, and J. Du, *Science* **347**, 1135 (2015).

[17] I. Lovchinskya, A. O. Sushkova, E. Urbach, N. P. de Leon, S. Choi, K. de Greve, R. Evans, R. Gertner, E. Bersin, C. Müller, L. McGuinness, F. Jelezko, R. L. Walsworth, H. Park, and M. D. Lukin, *Science* **351**, 836 (2016)

[18] C. Munuera-Javaloy, R. Puebla, B. D'Anjou, M. B. Plenio, and J. Casanova, arXiv preprint: 2110.14255 (2021).

[19] C. Munuera-Javaloy, R. Puebla and J. Casanova, *EPL* **134**, 30001 (2021)

[20] J. M. Boss, K. S. Cujia, J. Zopes, and C. L. Degen, *Science* **356**, 837 (2017).

[21] S. Schmitt, T. Gefen, F. M. Stürner, T. Unden, G. Wolff, C. Müller, J. Scheuer, B. Naydenov, M. Markham, S. Pezzagna, J. Meijer, I. Schwarz, M. B. Plenio, A. Retzker, L. P. McGuinness, and F. Jelezko, *Science* **356**, 832 (2017).

[22] D. R. Glenn, D. B. Bucher, J. Lee, M. D. Lukin, H. Park, and R. L. Walsworth, *Nature* **555**, 351 (2018).

[23] D. B. Bucher, D. R. Glenn, H. Park, M. D. Lukin, and R. L. Walsworth, *Phys. Rev. X* **10**, 021053 (2020).

[24] N. Arunkumar, D. B. Bucher, M. J. Turner, P. TomHon, D. Glenn, S. Lehmkuhl, M. D. Lukin, H. Park, M. S. Rosen, T. Theis, and R. L. Walsworth, *PRX Quantum* **2**, 010305 (2021).

[25] Ö. O. Soykal, P. Dev, and S. E. Economou, *Phys. Rev. B* **93**, 081207 (2016)

[26] Ö. O. Soykal, and T. L. Reinecke, *Phys. Rev. B* **95**, 081405 (2017)

[27] T. Maly, G. T. Debelouchina, V. S. Bajaj, K. Hu, G. Joo, M. L. Mak-Jurkauskas, J. R. Sirigiri, P. C. A. van der Wel, J. Herzfeld, R. J. Temkin, and R. G. Griffin, *J. Chem. Phys.* **128**, 052211 (2008)

[28] Q. Z. Ni, E. Daviso, T. V. Can, E. Markhasin, S. K. Jawla, T. M. Swager, R. J. Temkin, J. Herzfeld, and R. G. Griffin, *Acc. Chem. Res.* **46**, 1933 (2013)

[29] J. Casanova, E. Torrontegui, M. B. Plenio, J. J. García-Ripoll, and E. Solano, *Phys. Rev. Lett.* **122**, 010407 (2019)

[30] C. Munuera-Javaloy, Y. Ban, X. Chen, and J. Casanova, *Phys. Rev. Applied* **14**, 054054 (2020).

[31] M. Lee, and W. I. Goldburg, *Phys. Rev.* **140**, 1261 (1965)

[32] J. S. Waugh, L. M. Huber, and U. Haeberlen, *Phys. Rev. Lett.* **20**, 180 (1968)

[33] C. A. Meriles, L. Jiang, G. Goldstein, J. S. Hodges, J. Maze, M. D. Lukin, and P. Capellaro, *J. Chem. Phys.* **133**, 124105 (2010).

[34] F. Reinhard, F. Shi, N. Zhao, F. Rempp, B. Naydenov, J. Meijer, L. T. Hall, L. Hollenberg, J. Du, R.-B. Liu, and J. Wrachtrup, *Phys. Rev. Lett.* **108**, 200402 (2012).

#### Appendix A: Measured signal

After the triggering pulse with  $\phi = 0$ , the magnetization reads  $\mathbf{M} = (0, -1, 0)$ . This is the initial configuration for the first phase acquisition stage. The free precession stages (of fixed duration  $\tau$ ) split the magnetization in different components  $\mathbf{M}_k$  such that the initial configuration for the  $k^{\text{th}}$  spectral component at the  $n^{\text{th}}$  phase acquisition stage reads  $\mathbf{M} = (\sin(\delta_k n\tau), -\cos(\delta_k n\tau), 0)$ . This is obtained from the Bloch equations with  $\Omega = 0$ .

Now, the evolution of the magnetization during the  $n^{\text{th}}$  phase acquisition stage reads

$$\mathbf{M}_k^n(t) = \begin{pmatrix} 1 & 0 & 0 \\ 0 & \cos(\Omega t) & -\sin(\Omega t) \\ 0 & \sin(\Omega t) & \cos(\Omega t) \end{pmatrix} \begin{pmatrix} \sin(\delta_k n\tau) \\ -\cos(\delta_k n\tau) \\ 0 \end{pmatrix} = \begin{pmatrix} \sin(\delta_k n\tau) \\ -\cos(\delta_k n\tau) \cos(\Omega t) \\ -\cos(\delta_k n\tau) \sin(\Omega t) \end{pmatrix}. \quad (\text{A1})$$

Notice that the Bloch equations in the main text, and therefore the solutions obtained from them, describe the dynamics in a frame that rotates around the external field at the RF driving frequency  $\omega$ . For the sake of simplicity in the presentation, the

solution in Eq. (A1) assumes no decoherence (i.e.  $T_1, T_2 \rightarrow \infty$ ). However, the numerical simulations leading to the results displayed in the main text include realistic  $T_1$  and  $T_2$ , and hence imply numerically solving the Bloch equations in Eq. (1) of the main text. Here we show the approximate analytical solution to provide the reader with an insight on the dynamics at the phase acquisition stages of the protocol.

The interaction between the signal produced by the rotating  $\mathbf{M}_k^n(t)$  and the sensor in a rotating frame w.r.t. the NV electronic-spin ground-state triplet is

$$H/\hbar = -\gamma_e S_z B_n(t) + \Omega_{\text{MW}}(t) S_z. \quad (\text{A2})$$

Here  $\Omega_{\text{MW}}(t)$  is the MW control field, and the target signal induced by the  $n^{\text{th}}$  phase acquisition stage is  $B_n(t) = \sum_k B_k^n(t)$  such that

$$B_k^n(t) = \frac{\hbar^2 \gamma_N^2 \mu_0 \rho_k B_{\text{ext}}}{16\pi k_B T} \mathbf{M}_k^n(t) \int [g_x(r), g_y(r), f(r)] dV, \quad (\text{A3})$$

where  $\mu_0$  is the vacuum permeability,  $\rho_k$  the density of spins with the  $k^{\text{th}}$  precession frequency,  $\gamma_N$  is the nuclear gyromagnetic factor,  $T$  the temperature of the sample,  $k_B$  the Boltzmann constant, and  $B_{\text{ext}}$  the external magnetic field. The geometric functions  $g_{x,y}(r)$  and  $f(r)$  read

$$f(r) = \frac{1}{r^3} (3r_z^2 - 1) \quad \text{and} \quad g_{x,y}(r) = \frac{1}{r^3} (3r_z r_{x,y}), \quad (\text{A4})$$

with  $\hat{r} = (r_x, r_y, r_z)$  being the unitary vector joining the NV and  $dV$ , while  $r$  represents their relative distance. The expression in (A3) (which can be derived from a microscopic description of a system involving NVs and nuclear spins [33]) is valid provided that the external magnetic field  $B_{\text{ext}}$  is greater than the coupling strength, which allows to ignore the backaction of the sensor in the sample [34]. As we are in a large field regime, this condition is met. In addition, the contribution of the orthogonal components  $M_{k,x}^n(t)$  and  $M_{k,y}^n(t)$  to  $B_k^n(t)$  (which rapidly oscillate with the Larmor frequency  $\gamma_N B_{\text{ext}}$ ) can be safely neglected.

The MW control implements an XY4 dynamical decoupling sequence that modulates the interaction between target and sensor leading to

$$H/\hbar = \frac{2\gamma_e S_z}{\pi} \sum_k b_k \cos(\delta_k n\tau), \quad (\text{A5})$$

where  $b_k = \frac{\hbar^2 \gamma_N^2 \mu_0 \rho_k B_{\text{ext}}}{16\pi k_B T} \int f(r) dV$ .

The NV is initialized in the  $|+\rangle = \frac{1}{\sqrt{2}} (|1\rangle + |0\rangle)$  state, then evolves during  $t_m$ , and it is finally measured such that (in the small angle regime)

$$\langle \sigma_y \rangle_n = \frac{2\gamma_e t_m}{\pi} \sum_k b_k \cos(\delta_k n\tau). \quad (\text{A6})$$

On the other hand, an RF trigger pulse with  $\phi = \pi/2$  leads to  $\mathbf{M}_k = (1, 0, 0)$ , which yields a splitting of the  $k$  spectral components during the free precession stages described by  $\mathbf{M}_k = (\cos(\delta_k n\tau), \sin(\delta_k n\tau), 0)$ . For the same dynamical decoupling control sequence over NVs, we find

$$\langle \sigma_y \rangle_n = \frac{2\gamma_e t_m}{\pi} \sum_k b_k \sin(\delta_k n\tau). \quad (\text{A7})$$

## Appendix B: Radio field intensity estimation

In this section we estimate the radio signal amplitude for the example in the main text. We numerically compute the geometrical integral  $F = \int f(r) dV$  for different hemispheres while we consider the NV axis perpendicular to the diamond surface. This leads to an asymptotical value of  $F \sim 4.1$ . Note that half of the asymptotic value is reached for integration hemispheres with a radius of 2-3 times the depth of the NV, which leads to detectable signals even for picoliter volume samples. Considering a pure ethanol sample with a density of  $789 \text{ kg m}^{-3}$  and a molar mass of  $46 \text{ g mol}^{-1}$ , we obtain a proton density of  $\rho = 6.2 \times 10^{28} \text{ m}^{-3}$ . With this into account, the total amplitude obtained in a 2.1 T external field at room temperature is  $b \sim 2.56 \text{ nT}$ . Finally, we can distribute this amplitude throughout the ethanol spectral peaks according to the following rules:  $b/3$  (signal produced by 2 out of 6 hydrogens of the molecule) distributed in four peaks with ratios 1:3:3:1, a single peak of  $b/6$ , and  $b/2$  (signal produced by 3 out of 6 hydrogens of the molecule) distributed in three peaks with ratio 1:2:1, to obtain

$$b_k \in \{106, 320, 320, 106, 426, 320, 640, 320\} \text{ pT}. \quad (\text{B1})$$